Multi-Objective Design of a Line-Start PM Motor Using the Taguchi Method

A. J. Sorgdrager, *Member,* R-J. Wang, *Senior Member,* and A. J. Grobler, *Member, IEEE*

***Abstract*—This paper investigates the use of the Taguchi method for the design of line-start permanent magnet synchronous motors (LS-PMSMs). To address the inherent limitation of the Taguchi method in solving multi response optimization problems, an improved regression rate methodology and a weighted factor multi-objective technique are incorporated to form a Taguchi method based multi-objective design framework. To validate the proposed method a prototype machine has been designed, constructed and experimentally evaluated. It shows that the proposed method can effectively take into account both steady-state and transient synchronization performances in the design of LS-PMSMs.**

***Index Terms*—Line-start, permanent magnet motor, multi-objective optimization, synchronization, Taguchi method**

I. Introduction

UNLIKE conventional permanent magnet (PM) motors, a line-start PM synchronous motor (LS-PMSM) has a hybrid rotor containing both a squirrel cage and a PM array. This provides self-starting capability and enables synchronous operation at steady-state. When designing an LS-PMSM, both steady-state and transient operations need to be considered.

The transient state of an LS-PMSM is rather complex as the behavior of the machine is determined by the cage torque, the braking torque (due to the interaction between PMs and the stator winding) and the load torque as illustrated in Fig. 1. Apart from the load torque, the moment of inertia (J) [1], [2], the influence of reluctance torque and torque oscillations during starting [3] also significantly influence the transient synchronization performance of an LS-PMSM. Transient finite element (FE) modeling is usually required to accurately predict the synchronization status of an LS-PMSM. However, because of the high computational costs of the transient FE modelings, their application in an iterative design optimization is highly undesirable.

Alternative methods such as the analytical synchronization energy criteria [3]–[6], transient performance constraints [7], [8] or an FE-assisted analytical model [9] are proposed for the transient performance analysis of LS-PMSMs. These methods significantly reduce the high computational expenses associated with FE simulations making it viable to include transient performance calculation in a design optimization procedure. Some recently published work discusses the optimal design guidelines for LS-PMSMs considering both transient and steady-state characteristics [10]. Although extensive research has been conducted on the LS-PMSMs and their design aspects, little can be found in literature on the multi-objective optimal design strategy of LS-PMSMs.

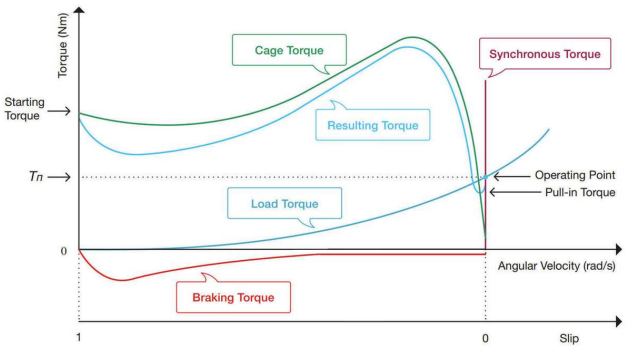

Fig. 1. LS-PMSM torque components as a function of slip [6].

In this paper, a Taguchi method based multi-objective design strategy is proposed for the design of LS-PMSMs. The use of Taguchi method in electrical machine design is relatively new [11]. The Taguchi method differs from commonly used optimization methods in that it analyzes the results to locate a region where the performance objective is most stable rather than searching for a definite point in the domain [2], [12]. Some key advantages of the Taguchi method are the independence from initial conditions, reduced parameter complexity, and relative ease with determining the subsequent conditions of the parameters in an iterative process. Traditionally, the Taguchi method is unsuitable for iterative and multi-objective design optimization (MODO) problems [13]. To address this limitation, an improved Taguchi method based regression rate (TBRR) optimization framework is proposed in this paper for LS-PMSM designs. The aim of the proposed method is to effectively take into account both steady-state and transient synchronization performances in the design of LS-PMSMs.

The rest of the paper is structured as follows. The functionality, limitations, improvements and the formulation of performance objectives of the TBRR optimization framework are described in Section II. The implementation of the TBRR method for the multi-objective optimization of a typical LS-PMSM topology for fan-load application is explained in Section III, from which a balanced optimal design is identified and verified using both analytical and 2D FE time-step performance calculations. Section IV reports the experimental investigation of an LS-PMSM prototype to assess the effectiveness of the

A. J. Sorgdrager and R-J. Wang are with the Department of Electrical and Electronic Engineering, Stellenbosch University, Stellenbosch, 7600, South Africa. e-mail: ajsorgdrager@gmail.com; rwang@sun.ac.za

A. J. Grobler is with School of Electrical, Electronic and Computer Engineering, North-West University, Potchefstroom, 2531, South Africa. e-mail: andre.grobler@nwu.ac.za

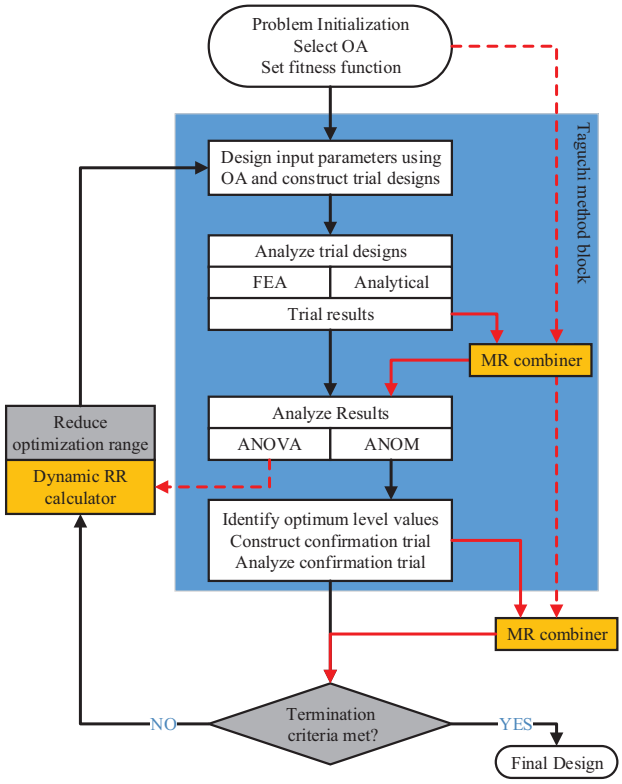

Fig. 2. Taguchi method based regression rate framework with proposed improvements.

proposed method and the performance objectives. Relevant conclusions are drawn in Section V.

II. Taguchi Method Based Regression Rate Framework

The TBRR optimization framework was originally proposed for antenna array optimization in [14]. Figure 2 illustrates the process flow of the TBRR design method, in which the two dark grey blocks enable an automated decision functionality for the Taguchi method block. This is achieved by including a fitness function as an overall evaluation criterion (OEC), a termination criterion and a dedicated method to adjust each parameter's range for the subsequent iteration. The black arrows indicate the sequence of functions of the original TBRR method as in [14]. A brief description of the functionality of each block in Fig. 2 is given below:

• *Problem initialization*: The optimization procedure starts with the problem initialization, which includes the selection of design parameters (e.g. rotor dimensions) and a suitable orthogonal array (OA), defining parameter range, and the formulation of a fitness function. The range of a parameter is vital as all the trial designs (as specified by the OA) must be viable. Taguchi's OA design is based on a design matrix considering only a selected subset of combinations of multiple factors at multiple levels [12]. The selection of an OA mainly depends on the number of parameters. The fitness function is devised according to the optimization objective and is either maximized or minimized depending on the goal.

• *OA input parameter allocation and trial construction*: For an iteration, the numerical values for each level of a parameter must be determined in order to conduct the trials. For the first iteration (if a 3-level parameter OA is used) the maximum and minimum range values of the n^{th} parameter, $Pn_{\max}$ and $Pn_{\min}$, is allocated to level-1 and level-3, respectively, thus, level-2 will be the mid-range value between the two boundaries. The difference between any two levels is known as the level difference (LDn). For the first iteration, LDn_1 is determined by the following equation:

$$\text{LDn}_1 = \frac{Pn_{\max} - Pn_{\min}}{\text{number of levels} + 1} \tag{1}$$

For the subsequent iterations, LDn_i is reduced after each iteration until the termination criteria are met. By reducing the level difference between two levels, the parameter's range is also reduced.

• *Analyze trial designs* and *Analyze results*: Once all the OA's trials have been compiled and conducted, the relative information for the fitness function of each trial must be obtained. The fitness function performance of a given trial is used to build the Analysis of Mean's (ANOM) response table. The ANOM is formulated using the Signal-to-Noise (S/N) ratio values of the fitness function and is used to identify the optimum conditions of each parameter by studying the main effects of each level [11], [12]. A detailed example of implementing Taguchi method in electrical machine designs can be found in [2].

• *Optimal level identification and confirmation experiment*: As the S/N ratio analysis is used, the optimum condition for each parameter is identified by the largest S/N ratio value. A confirmation trial is performed using each of the optimum level conditions, under the same circumstances as the main OA trials. This is done to determine the fitness value of the current iteration.

• *Check the termination criteria*: The optimization is terminated when the fitness function has converged over several iterations and/or when the level difference (LD) ratio is less than the converged value (CV) set by the designer. The latter is used as a termination criterion for the optimization procedure in this study, i.e.

$$\frac{\text{LDn}_i}{\text{LDn}_1} < \text{CV} \tag{2}$$

with CV selected between 0.001 and 0.01. With the parameter level values closer to each other, the current fitness value should also be close to the previous value, thus, converging around the optimum point.

• *Reduce the optimization range*: If another iteration is required due to the termination criterion/criteria not being met, the range of each current parameter must be reduced, which is done by multiplying the current LD with a regression rate (RR) factor as follows:

$$\text{LDn}_{i+1} = \text{RR} \cdot \text{LD}_i \tag{3}$$

For the next iteration, the current optimum value is placed in the level-2 slot. Level-1 and level-3 values are calculated with the new LD determined from (3). To ensure that the new level values are within the original range of the parameter, a process of checking these values is necessary as discussed in [2].

A. The Limitations of the Existing TBRR Method

In the originally proposed TBRR method [14], the OEC was only formulated for a single-objective optimization, which is unsuitable for multi-objective optimization problems. Secondly, a fixed regression rate was used for all the design parameters, which is not ideal as the regression rate has a direct impact on either the computational efficiency or the confidence in optimization results.

B. Enabling Multi-Objective Optimization

To enable the multi-objective optimization, two improvements to the original TBRR method are proposed in this paper. Firstly, the inclusion of a Multi-Response (MR) combiner to enable the method with MODO capabilities, and secondly, the use of a dynamic RR (RR_{dyn}) by actively linking a parameter's RR to its percentage contribution towards performance variance. The latter is calculated by the Analysis of Variance (ANOVA), which forms part of the Taguchi method methodology. The two newly introduced function blocks are highlighted in Fig. 2 with the deviations in the design flow shown by the red (gray if in gray scale) arrows. The dashed arrows indicate the information sharing paths.

As described in [13], different methods can be applied for a MR combiner to incorporate multiple objectives into a single OEC. The two MR combiner blocks in Fig. 2 are independent from each other. The first MR combiner is used to combine the selected performance objective for each trial design from the selected OA and forms part of the Taguchi method block. The second MR combiner block combines the confirmation trial's performance objectives into a single response, which is tested against the termination criteria.

For the design of an LS-PMSM, the performance characteristics of the steady-state and transient state may be treated as individual design objectives, which are combined inside the MR combiner blocks using the weighted function below:

$$\text{OEC} = f(w_1, w_2) = w_1\overline{\text{SS}} + w_2\overline{\text{TS}} \tag{4}$$

where $w_1 + w_2 = 1$, $\overline{\text{SS}}$ and $\overline{\text{TS}}$ are the normalized steady-state and transient performances, respectively. To normalize each objective, SS_{max} and TS_{max} need to be found, which entails the formulation and evaluation of two single-objective OECs, i.e. MAX(SS) and MAX(TS). With the knowledge of the maximum objective values, SS_{max} and TS_{max}, (4) can be rewritten as

$$\text{OEC} = f(w_1, w_2) = w_1 \frac{\text{SS}}{\text{SS}_{\text{max}}} + w_2 \frac{\text{TS}}{\text{TS}_{\text{max}}} \tag{5}$$

By normalizing each state, equal representation is ensured when combining the two states. To evaluate the influence of the weights, w_1 and w_2, a Pareto optimization can be particularly useful [15].

C. Performance Objectives

The performance objectives for both steady-state and transient state operations of the LS-PMSMs are described below:

• *Steady-State Objective*: LS-PMSMs are mainly used in fixed speed applications such as fans or pumps, thus the rated power factor and efficiency are important design considerations. Since the power factors of LS-PMSMs correlate with efficiencies [10], [16], the power factor was chosen as the steady-state performance objective in this study. This is also because the power factor shows a clear competing relationship with the transient performance parameters [10]. The analytical steady-state performance calculation of an LS-PMSM employing equivalent circuit equations was conducted by using ANSYS RMxprt package at full-load conditions.

• *Transient Objective*: Since the transient starting and synchronization capability of LS-PMSMs are closely related to the system moment of inertia [3]–[6], the maximum inertia that an LS-PMSM can successfully synchronize is used for quantifying the transient performance. Using the time-domain formulation of the energy-based analytical synchronization model in [6], the speed versus time characteristics and the synchronization capability of the LS-PMSM for a given load and moment of inertia can be obtained. Synchronization is determined by applying two simple rules:

- An LS-PMSM is considered synchronized when the mean value of the speed and its 1st order derivative at the last part of the time interval equal to synchronous speed and zero, respectively;
- An LS-PMSM is considered unsynchronized when its speed oscillates below synchronous speed.

For the same load torque-speed profile, the maximum load inertia J_{cr} that a candidate machine can successfully synchronize can be expressed as:

$$J_{cr} = x_{cr} J_{\text{rotor}} \tag{6}$$

where J_{rotor} is the rotor inertia and x_{cr} is the critical inertia factor of a candidate machine. In the case that the rotor volume is not fixed, the rotor inertia of an equivalent induction machine may be used as the normalization value.

To find x_{cr}, a range-based search method is employed as discussed in [17]. This approach reduces the overall execution time required over the optimization process as the number of calls for synchronization model is significantly less for a set of candidate machines. For this method, the maximum load synchronization capability needs to be set by the designer. Since LS-PMSMs have poorer load synchronization capabilities than induction machines (IM), the x_{cr} of an equivalent IM can be used as a benchmark.

In the case that a candidate machine fails to synchronize with the load $J_{\text{cr}} = J_{\text{rotor}}$, the Taguchi analysis still requires a set value. As a zero value trial set cannot be included in the S/N analysis, the minimum critical inertia for such a candidate machine is set to 1.

D. Dynamic Regression Rate

As discussed in [2], the selection of RR value has much influence on both the number of iterations and the performance correlation in the Taguchi method based optimization problems. A large RR leads to a slower LD convergence, thus, a higher number of iterations before termination, while a lower RR value generally results in less number of iterations. However, an optimization with a lower RR value is more likely

TABLE I
KEY LS-PMSM DESIGN SPECIFICATIONS

Description	Stator	Rotor
Outer diameter (mm)	160	99.4
Inner diameter (mm)	100	26
Stack length (mm)	120	120
Winding type	Lap	Cage
Number of slots	36	28
Core material	M400-50A	M400-50A
Magnet type	-	N48H
Rotor bars	-	1050 alloy
Moment of inertia (kg.m^2)	-	0.009

TABLE II
SELECTED DESIGN PARAMETERS.

Parameter	Description	OA
D1Dc	Saturation zone between cage and PM duct regions	P1
D1	Boundary between cage and PM duct regions	P2
Rib	Tangential distance between two PM ducts	P5
H1	Cage slot shoe height	P6
H2	Cage slot tooth height	P7
B1/B2	Cage slot tooth width	P8
PMt	PM thickness	P3
PMw	PM width	P4

to realize a less favorable design than that of an optimization with a higher RR value. To address this, the feedback from the ANOVA is used to adapt the regression value between a minimum (RR_{min}) and maximum (RR_{max}) value. This dynamic regression RR_{dyn} is linked to a parameter's contribution towards performance variance and is calculated using

$$RR_{dyn} = [RR_{max} - RR_{min}] \frac{\sigma^2}{100} + RR_{min} \tag{7}$$

where σ^2 is the percentage contribution towards performance variance obtained from the ANOVA analysis. It is clear from (7) that the higher the variance contribution is, the higher RR_{dyn} becomes. In addition, the formulation of (7) ensures that RR_{dyn} will never be less than RR_{min}. With these proposed improvements, the enhanced TBRR method can be readily applied to MODO problems.

III. IMPLEMENTATION OF THE TBRR METHOD

For the design study a 4-pole, 525 V, 2.2 kW, premium efficiency induction machine is used as the base machine. The basic design specifications of LS-PMSM are summarized in Table I. The layout of the PM array and cage slot of the LS-PMSM rotor are given in Fig. 3(a) and 3(b), respectively, where the selected per unit design parameters (underlined) are described in Table II and the Appendix. The aim of the study is to find the best suited design for a typical fan-load application.

For this implementation of the TBRR method, the cage and PM duct parameters are included in an L18 OA. The placement of the parameters in the OA is described in Table II. To simplify the design and to ensure equal representation when calculating the current LD using (2), per unit parameter values (x_{pu}) is used in the design equations. Each design parameter as selected in Table II is represented by x_{pu} values (ranging initially between 0 and 1) in the selected OA. After each iteration the TBRR method reduces the per unit range of each corresponding x_{pu} parameters accordingly until termination.

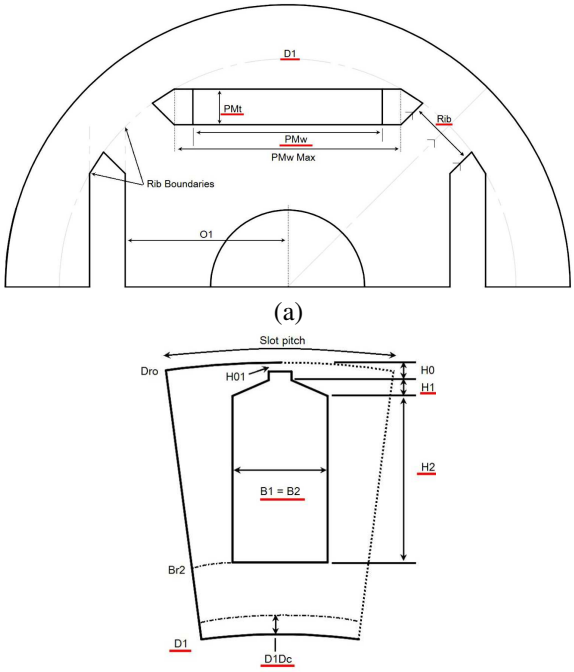

Fig. 3. LS-PMSM rotor layout and design parameters: (a) radial flux PM topology (b) block-type rotor slot.

For each candidate design, the steady-state and transient performance analyses were conducted by using the analytical models described in [2], [6]. Since an optimum design may be susceptible to the influences of uncontrollable non-design factors (noise factors), it is important to realize a robust design that is less sensitive to noise factors. One of the key advantages of the Taguchi method is the provision to expose the designs to an outer noise array to ensure a more robust design. Per definition these noise factors should be of a direct influence on the performance objectives of the design, known to the designer, but also uncontrollable (e.g. manufacturing tolerances, variance in material properties) [12]. For this study the conductivity of the rotor bar material, the rotor diameter, the PM remanent flux density and field intensity are chosen as noise factors. A total of 76 design analyses per iteration is required for this design optimization problem, of which 72 (L18×L4) are main design trials and 4 (1×L4) are optimum design trials. Obviously, utilizing an outer noise array would increase the number of design trials. It should be noted that all the trial designs in Taguchi method are predefined per iteration, which can reduce the computational time of the design optimization by taking advantage of parallel computing process.

A. Pareto Optimum

In a multi-objective optimization problem, it is generally not feasible to find a design that maximizes all the objectives of the problem. Instead, the aim is rather to find a judicious tradeoff among all the objectives of a given OEC, which is known as the Pareto optimum [18] of the OEC. For each weighted combination of $w_1 + w_2 = 1$ there exists a Pareto optimum. All

the Pareto optimal points lie on the boundary of the possible solution space. Using the selected performance objectives, the OEC for the design optimization can be expressed by:

$$\text{OEC} = f(w_1, w_2) = w_1 \frac{\text{PF}}{\text{PF}_{\text{max}}} + w_2 \frac{x_{cr}}{x_{cr\,\text{max}}} \tag{8}$$

After the maximum values of both the PF and x_{cr} are obtained as required in (8), w_2 is incremented from 0.1 to 0.9 in steps of 0.1 with $w_1 = 1 - w_2$. For each combination of $f(w_1, w_2)$ the optimum and robust designs are realized using the TBRR method. To identify the robust design, the Taguchi method uses the Signal-to-Noise (S/N) ratio to analyze the results.

Along with the Pareto front, the relationship between the weighted-factor OEC and weights can also be plotted. The weighted-factor OEC function attains a maximum at $f(1, 0)$ and $f(0, 1)$, where the OEC essentially reduces to a single objective function. When both objectives are considered during the optimization, the TBRR method searches for a balanced optimum design. Since there exists a balanced Pareto optimum, the same point must be present on the weighted-factor OEC function plot curve [18], [19]. This point is represented by the single minimum performance point on the function plot, which indicates the maximum sacrifice each objective concedes. The function plot follows the same Pareto optimality logic whereby the maximum performance of any of the two maximums is sacrificed to improve the other objective. The weighted combination of $w_1 = 1 - w_2$ at the minimum point is determined by finding the zero gradient point of (8) [19]. In the event of a weak Pareto optimum or a complementing relationship this approach may not be valid. Thus, it is important that both these criteria are met.

B. Optimization Results

Upon completion of the optimization, the steady-state and transient performances of each candidate / trial machine generated by the TBRR method is used to construct a Pareto domain in relation to both the PF and J_{cr} (Fig. 4). In the figure, J_{cr} is calculated by multiplying x_{cr} of each trial machine with the rotor inertia J_{rotor}. Both the robust and global average optimums are highlighted on the Pareto front. From Fig. 4 it can be seen that there clearly exists a competing relationship between the two objectives, J_{cr} and PF. This can also be seen by plotting the weighted-factor objective function of either the robust or optimums realized by the TBRR method as in Fig. 5.

For the case presented in the figure the balanced optimum design for the MODO problem can be determined when $w_1 = 0.64$ and $w_2 = 0.36$, which corresponds to $f(w_1, w_2)' = 0$ in Fig. 5 (indicated by a large black dot). The cross-sections of the designs ranging from $f(0, 1)$ to $f(1, 0)$ are presented together with the balanced optimum design (shaded) in Fig. 6. Their respective values of design parameters are given in Table III together with the initial design values. It can be observed from the cross-sections that the change in PM volume is more significant than in rotor slots as the weight is shifted. This highlights the performance dependence of both steady-state and transient operations on the PM volume. The optimum design is also highlighted on the Pareto front in Fig. 4, which

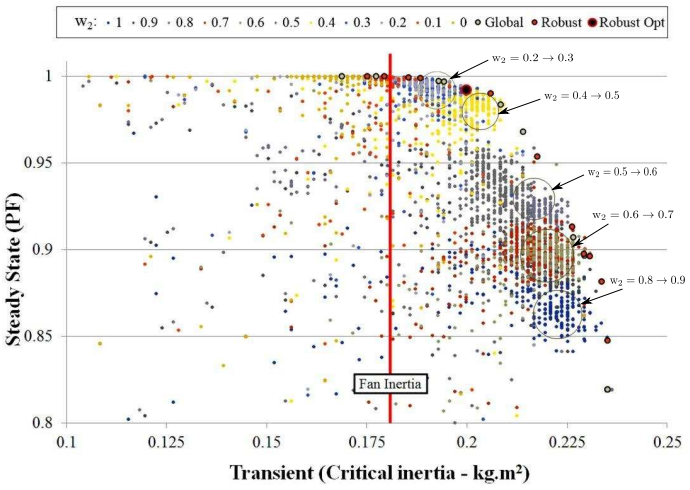

Fig. 4. Pareto front using OA trial, optimum and robust design results

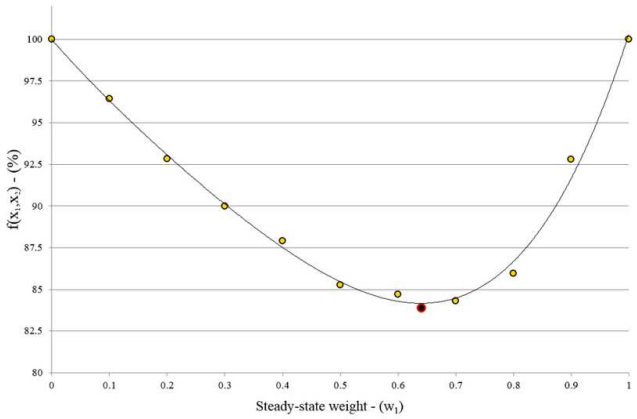

Fig. 5. Weighted-factor objective function plot of the robust optimums.

is sightly biased toward the steady-state performance, but with satisfactory synchronization capabilities. The optimum machine has a calculated PF of 0.98, efficiency of 89.2% and J_{cr} of 0.205 kg.m^2.

To verify the J_{cr} of the balanced optimum design, ANSYS Maxwell 2D transient FEM simulations are utilized to inspect the synchronization capabilities of the design. For the verification, the design is subjected to the four outer OA noise conditions used in the TBRR optimization. The synchronization status of the design is simulated with the moment of inertiae of the load at $J_{cr} \pm 5\%$. For the design to be deemed fit, it should attain synchronized and unsynchronized states under all four outer noise conditions when the inertia of the load is 5% below and above J_{cr}, respectively. The speed-time curves of the eight simulations are presented in Fig. 7, where it can be seen that the corresponding synchronized and unsynchronized states for both load inertia values are as expected.

IV. Experimental Investigation

The purposes of the experimental investigation are first to validate the effectiveness of the TBRR method as a design optimization method and second to verify if x_{cr} is an appropriate

TABLE III
OPTIMIZED PARAMETER VALUES FOR FIG. 6 (IN MM).

Parameters	Initial values	f(0,1)	f(0.1,0.9)	f(0.2,0.8)	f(0.3,0.7)	f(0.4,0.6)	f(0.5,0.5)	f(0.6,0.4)	**f(0.64,0.36)**	f(0.7,0.3)	f(0.8,0.2)	f(0.9,0.1)	f(1,0)
D1Dc	1	1	1	1	0.799	0.799	0.700	0.712	**0.700**	0.600	0.600	0.613	0.600
D1	50	73.54	73.87	74.87	74.55	73.95	74.23	74.83	**75.33**	76.57	76.87	77.11	78.21
Rib	2	2	2.224	2,676	2.825	2.8135	2.912	2.939	**2.998**	2.990	2.978	2.930	3
H1	10	0.051	0.0552	0.0615	0.832	0.901	0.914	0.926	**0.965**	0.911	0.925	0.769	0.727
H2	20	10	9.751	9.516	8.482	8.759	8.567	8.823	**8.713**	8.018	8.021	7.837	7.419
B1/B2	5	5.442	5.226	5.242	5.117	4.977	5,016	5.187	**4.958**	5.171	5.183	4.703	4.381
PMt	3	4	4.341	4.676	4.764	4.917	4.821	4.803	**5.768**	5.960	6	6	6
PMw	25	20.47	21.76	23.23	24.38	24.77	24.87	25.19	**28.25**	29.70	29.85	30.46	31

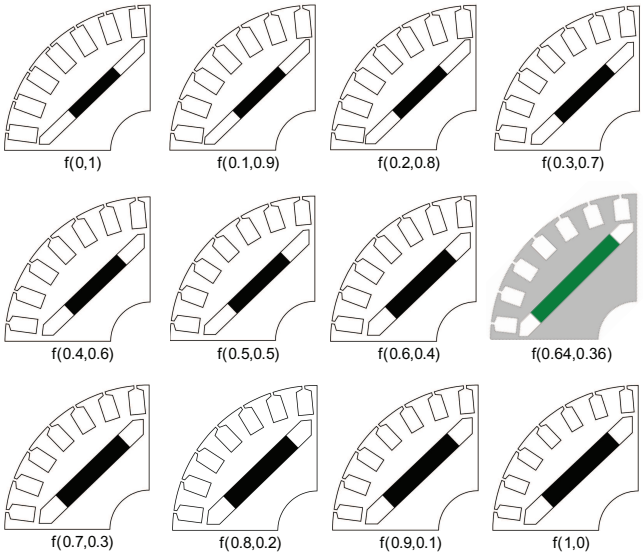

Fig. 6. Cross-sections of the LS-PMSM designs for $f(0,1)$ to $f(1,0)$.

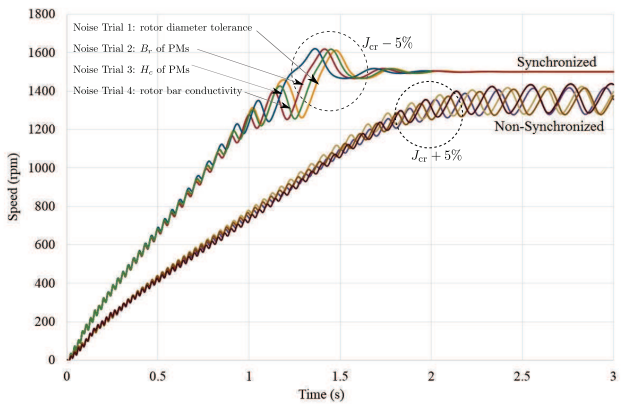

Fig. 7. Transient FEM simulations of the balanced design to verify the design's synchronization capabilities.

design objective for transient performance.

Because of the limited size range of the flat aluminum bars and their poor machinability, the balanced optimum design realized by the TBRR method could not be manufactured within the allotted budget. An alternative design within the Pareto domain is selected. The rotor lamination of the manufactured prototype is shown in Fig. 8. To better understand the influence of the PMs on the synchronization, three design variants are devised, which are realized by using the PMs with different widths (*PMw* as shown in Fig. 3(a)) in the rotor. The PM widths for the three design variants, M1, M2 and M3, are 20 mm, 30 mm and 40 mm, respectively. Although the optimum design cannot be prototyped, the measured performance of the selected design should still show good correlation with the predicted steady-state performance and the corresponding synchronization status for the fan-load used in the optimization.

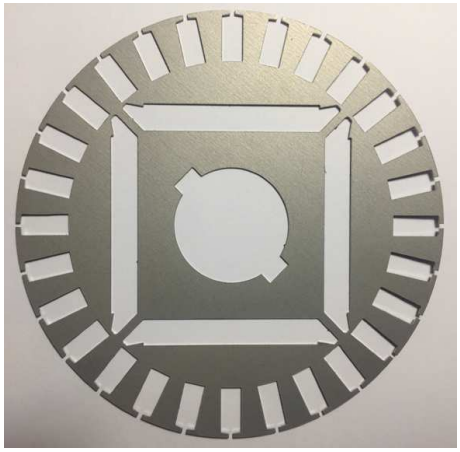

Fig. 8. The rotor lamination of the Prototype LS-PMSM.

To verify the use of analytically calculated critical inertia factor, x_{cr}, as a transient performance objective in a design optimization, the critical inertia factors for the prototype machines under different load conditions are experimentally determined and compared with the analytically calculated values. This will show the accuracy and viability of using analytically computed x_{cr} to represent the synchronization performance in the multi-objective optimization of LS-PMSMs.

A. Test Set-up and Variable Inertia Jig Design

To obtain the results required for the investigations, three test set-ups are devised as illustrated in Fig. 9. To determine the steady-state performance, the commonly used back-to-back set-up is implemented as in Fig. 9(a). A Fluke Norma 5000

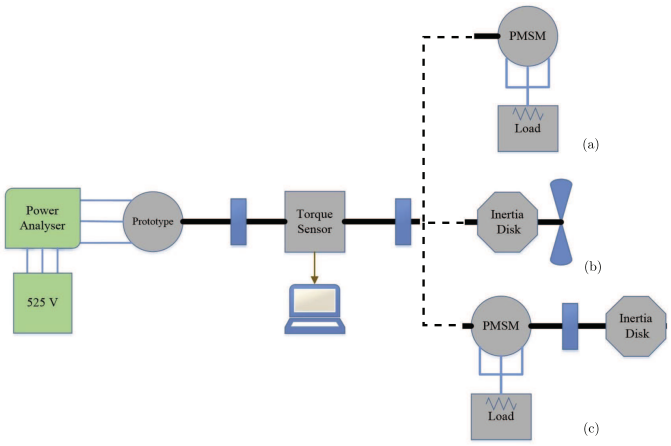

Fig. 9. Proposed test set-ups for: (a) Steady-state, (b) Fan-load synchronization, and (c) Critical inertia synchronization experimental investigations.

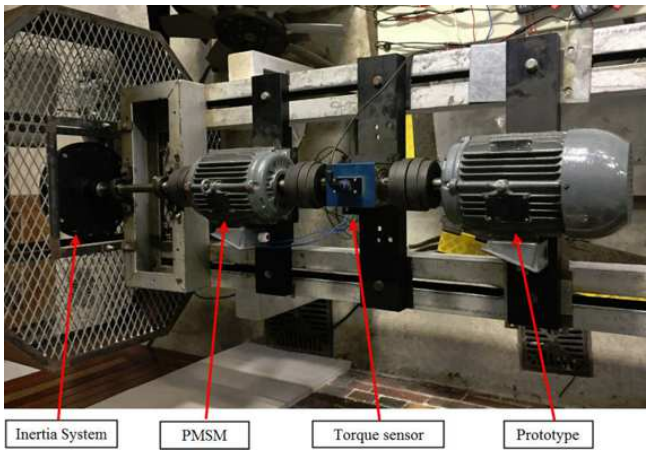

Fig. 10. Lab test set-up for determining the critical inertia at various loads (top view).

power analyzer is used to measure the input electrical power and power factor (PF) at rated conditions. A Lorenz Messtechnik GmbH DR-3000 torque sensor is used for the output torque and speed measurements. The prototype is loaded by means of a PMSM operating as a generator feeding resistive loads.

For the fan-load synchronization tests the set-up illustrated in Fig. 9(b) is employed. The full-load torque of the custom-made fan whose load characteristics are used in the design optimization is 14.25 Nm at synchronous speed (1500 rpm). The drive-train has a total inertia of 0.18 kg.m^2, which is also indicated on Fig. 4. To determine the load synchronization capabilities of the prototypes, a specially designed variable inertia system as shown in Fig. 9(c) is used to adjust the system inertia without influencing the applied load. The variable inertia system consists of a high density polyethylene base disk, several removable mild steel disk weights (fastened onto the base disk) and smaller point weights. The range of the system inertia can be adjusted up to 0.35 kg.m^2 in increments of 0.0025 kg.m^2. A photo of the lab test set-up for determining the load synchronization capabilities of the prototypes is shown in Fig. 10, where the variable inertia disk system is shown on the left. For the test, the adjustable resistive braking load is connected to the PM synchronous generator before the LS-PMSM prototype is started, which emulates the dynamic behavior of fan loads. The aim is to experimentally determine the critical inertia factor x_{cr} for different loads.

B. Comparison of Results

The calculated and measured performances of the prototype machines are compared and discussed in this section. For the test of the IM, the pitch angle of the fan blades is adjusted to ensure the same output power at its rated speed. Table IV summarizes the steady-state performances of the three design variants, M1, M2 and M3, and the base IM. Although the efficiency (η) and line current (I_{line}) of the machines were not the performance objectives in the OEC, they are also listed in the table for comparison. Clearly there exists a good correlation for the steady-state performances between the analytically calculated and measured results. Also included

TABLE IV
PERFORMANCE COMPARISON BETWEEN CALCULATED AND MEASURED OUTPUTS.

		η [%]	PF	P_{out} [W]	I_{line} [A]	Speed [rpm]	Synchronize?
M1	Calculated	87.48	0.54	2196	4.88	1500	Yes
20 mm	Measured	85.74	0.55	2197	4.89	1500	Yes
M2	Calculated	89.06	0.81	2199	3.20	1500	Yes
30 mm	Measured	89.13	0.79	2200	3.28	1500	Yes
M3	Calculated	88.81	1	2200	2.60	-	No
40 mm	Measured	89.50	1	2200	2.58	-	No
IM	Calculated	87.50	0.80	2200	3.30	1450	-
-	Measured	88.50	0.78	2196	3.34	1435	-
Test Set-up		Fig. 9(a)				Fig. 9(b)	

in Table IV is the predicted and experimentally determined fan-load synchronization status for all design variants. It can be seen that for each design variant the prediction from the analytical synchronization model has a good agreement with that of the lab test. The measured speed-time and torque-speed curves of the three design variants are shown in Fig. 11 and Fig. 12, respectively. The speed-time characteristic of the original IM is also given in Fig. 11, which shows an excellent

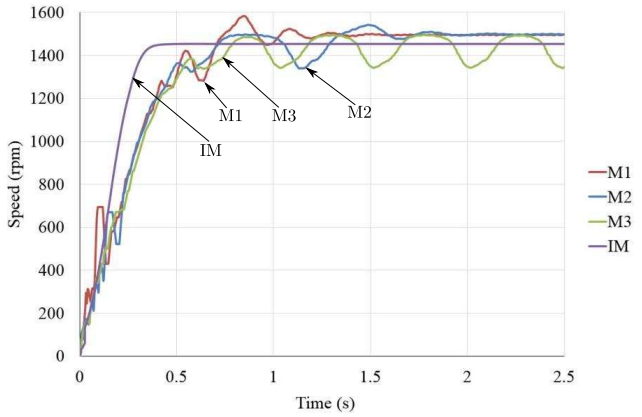

Fig. 11. Measured speed-time curves of each machine under investigation.

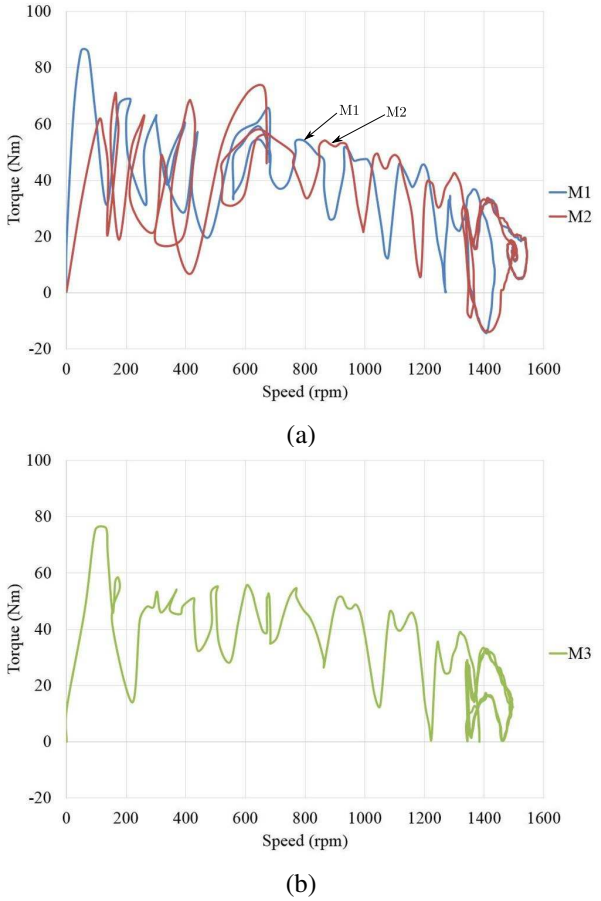

Fig. 12. Measured torque-speed curves of each machine under investigation (a) synchronized (b) un-synchronized cases.

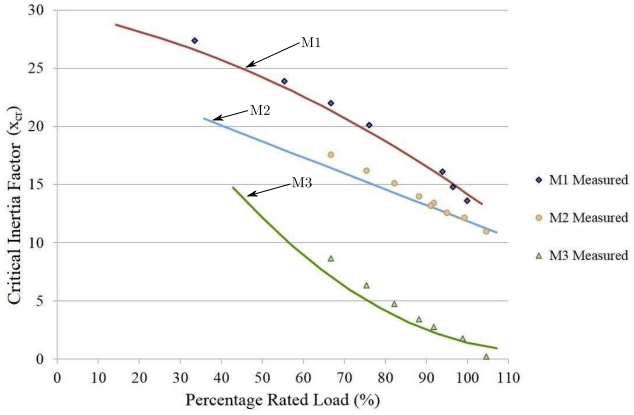

Fig. 13. Comparison of calculated (solid lines) and measured critical inertia as a function of percentage rated load.

transient performance.

To compare the load inertia synchronization capabilities of each design variant, the critical inertiae under different load conditions are experimentally determined. For each specific load condition J_{cr} can be found by gradually increasing system inertia to a maximum synchronizable value. This value is then normalized with regard to rotor inertia to determine x_{cr}.

In Fig. 13, the calculated (solid line) and measured x_{cr} of each LS-PMSM design variant are presented as a function of the percentage rated load. A good correlation between the calculated and measured values of x_{cr} between 80% to 105% rated load is evident. Below 80% rated load, the results show slightly poorer correlation, but still follow the same upwards trend. This can be expected as the steady-state machine parameters were used in the analytical synchronization analysis. It can be clearly observed that the synchronization capabilities of the LS-PMSMs are greatly influenced by the amount of PM material used. Designs with large amount PM material (e.g. M3) result in poorer load synchronization performance.

Based on the above comparison, it can be seen that the analytical machine model used to determine the steady-state performance is an accurate representation of a LS-PMSM. Furthermore, the good correlation between the calculated and measured values of x_{cr} also confirms the accuracy and the effectiveness of the analytical synchronization model proposed in [6]. As there exists a good correlation between the predicted and measured results for both steady-state and transient performances, it can be inferred that the analytical machine models used in the TBRR optimization framework are adequate.

V. Conclusion

This paper proposes the use of the TBRR method for the multi-objective design optimization of LS-PMSMs considering both steady-state and transient performances. To address the inherent limitation of the Taguchi method for MODO problems, novel techniques such as dynamic regression rate and multi-response combiner are incorporated into the proposed TBRR framework. To validate the proposed method a prototype machine has been designed, manufactured and experimentally evaluated. It shows that the proposed method can effectively take into account both steady-state and transient synchronization performances in the design of LS-PMSMs. It was also re-affirmed that there exists a competing relationship between the PF and J_{cr}. The TBRR method can accurately identify both global and robust optimum designs on the Pareto front. The analytical calculation of J_{cr} shows good agreement with that of the measured one close to rated load conditions. This confirms that the J_{cr} of an LS-PMSM can be used as a performance objective in the TBRR design optimization method.

Appendix A
Design Equations

A typical LS-PMSM rotor, as in Fig. 3(a), consists of cage winding and PM duct regions. The boundary between them is defined by:

$$D_1 = (D_{ro} - D_{ri})x_{\text{pu}} + D_{ri} \tag{9}$$

where D_{ro} and D_{ri} are the rotor and shaft diameters. Along with D_1, three parameters are required to characterize each of the PM duct and rotor cage. For the PM duct the *PMt*, *PMw* and the gap between two ducts (Rib) are used, which are represented by following equations:

$$PMt = PMt_{\text{max}}\, x_{\text{pu}} \tag{10a}$$

$$PMw = PMw_{\text{max}}\, x_{\text{pu}} \tag{10b}$$

$$Rib = 2\left(Rib_{\text{max}} - |Rib_{\text{bottom}} - Rib_{\text{top}}|\right) x_{\text{pu}} \tag{10c}$$

O_1 is so defined that the duct spans the maximum possible tangential width of the pole and is calculated with:

$$O_1 = \frac{1}{2}\left[D_1 \sin(\pi/4) - \textit{PMt}\right] \tag{10d}$$

The calculation of Rib and *PMw* is more complicated as some dimensional limits (e.g. $\textit{PMw}_{\text{max}}$) need to be complied. For $\textit{PMw}_{\text{max}}$, two possible half slot lengths, x_t and x_b, need to be evaluated using the mathematical relations below. The smallest of the two is then multiplied by two to find $\textit{PMw}_{\text{max}}$.

$$x_t = \sqrt{\left(D_1/2\right)^2 - (O_1 + \textit{PMt})^2} \tag{11a}$$

$$x_b = \sqrt{\left(D_1/2\right)^2 - O_1^2} \tag{11b}$$

To ensure the geometric validity of *Rib*, several boundaries need to be established and tested against, which are:

$$Rib_{\text{min bound}} = \frac{D_1}{2}\sin(\pi/4) \tag{12a}$$

$$Rib_{\text{top bound}} = \sqrt{\left|\left(D_1/2\right)^2 - (O_1 - \textit{PMt})^2\right|} \tag{12b}$$

$$Rib_{\text{bottom bound}} = \sqrt{\left|\left(D_1/2\right)^2 - O_1^2\right|} \tag{12c}$$

If either $Rib_{\text{top bound}}$ or $Rib_{\text{bottom bound}}$ is greater than $Rib_{\text{min bound}}$, that value is then replaced with $Rib_{\text{min bound}}$. The top and bottom *Rib* values are calculated from these boundary values as follow. The larger value between the two is used for Rib_{max} in (10c).

$$Rib_{\text{top}} = (O_1 + \textit{PMt} - Rib_{\text{top bound}})\sin(\pi/4) \tag{13a}$$

$$Rib_{\text{bottom}} = (O_1 - Rib_{\text{bottom bound}})\sin(\pi/4) \tag{13b}$$

For this study the block type slot is selected for rotor as shown in Fig 3(b) and flat aluminum bars are used for cage winding.

The main slot height is expressed as a function of H_{slot}.

$$H_{\text{slot}} = (D_{ro} - D_1)/2 - D_1 D_c \tag{14}$$

which is the radial length of the cage region excluding a small mechanical linkage $D_1 D_c$. The key slot parameters are calculated as follows:

$$H_2 = H_{\text{slot}} x_{\text{pu}} \tag{15a}$$

$$H_1 = (H_{\text{slot}} - H_2) x_{\text{pu}} \tag{15b}$$

$$H_0 = (H_{\text{slot}} - H_1 - H_2) x_{\text{pu}} \tag{15c}$$

The widths of the slots, B_1 and B_2, are a function of the number of slots, *Q* and the specific radius, B_{radi}. For the block type slot $B_1 = B_2$, only one of the two widths needs to be calculated.

$$B_2 = \frac{2\pi B_{\text{radi}}}{Q} x_{\text{pu}} \tag{16}$$

with $B_{\text{radi}} = D_{si}/2 - (H_0 + H_1 + H_2)$

ACKNOWLEDGMENT

This work is supported in part by Sasol Group Technology (Pty) Ltd, Stellenbosch University and North-West University (Potchefstroom Campus), all of South Africa.

REFERENCES

[1] C. Jedryczka, R. M. Wojciechowski, and A. Demenko, "The influence of squirrel cage geometry on synchronization of line start permanent magnet synchronous motor," *9th IET International Conference on Computation in Electromagnetics (CEM 2014)*, London, 31 Mar. - 1 Apr. 2014, pp. 1-2.

[2] A. J. Sorgdrager, *Design of line-start permanent magnet synchronous machines using the Taguchi method*, PhD dissertation, Stellenbosch University, Stellenbosch, South Africa, 2017.

[3] A. Takahashi, S. Kikuchi, K. Miyata, and A. Binder, "Asynchronous torque of line-starting permanent-magnet synchronous motors," *IEEE Trans. Energy Convers.*, vol. 30, no. 2, pp. 498-506, Jun. 2015.

[4] T. J. E. Miller, "Synchronization of line-start permanent magnet AC motors," *IEEE Trans. Power App. Syst.*, vol. 103, no. 7, pp. 1822-1828, Jul. 1984.

[5] S. F. Rabbi and M. A. Rahman, "Critical criteria for successful synchronization of line-start IPM motors," *IEEE J. Emerg. Sel. Topics Power Electron.*, vol. 2, issue 2, pp. 348-358, Jun. 2014.

[6] A. Chama, A. J. Sorgdrager, and R-J. Wang, "Analytical synchronization analysis of line-start permanent magnet synchronous motors," *Progress In Electromagnetics Research M, (PIER M)*, vol. 48, pp. 183-193, 2016.

[7] W. H. Kim, K. C. Kim, S. J. Kim, D. W. Kang, S. C. Go, H. W. Lee, Y. D. Chun, and J. Lee, "A study on the optimal rotor design of LSPM considering the starting torque and efficiency," *IEEE Trans. Magn.*, 45(3): 1808-1811, Mar. 2009.

[8] Ł. Knypiński, L. Nowak, and C. Jedryczka, "Optimization of the rotor geometry of the line-start permanent magnet synchronous motor by the use of particle swarm optimization," *COMPEL - The International Journal for Computation and Mathematics in Electrical and Electronic Engineering*, vol. 34, issue. 3, pp. 882-892, 2015.

[9] D. Mingardi and N. Bianchi, "Line-start PM-assisted synchronous motor design, optimization, and tests," *IEEE Trans. Ind. Electron.*, vol. 64, no. 12, pp. 9739-9747, Dec. 2017.

[10] E. Sarani and S. Vaez-Zadeh, "Design procedure and optimal guidelines for overall enhancement of steady-state and transient performances of line start permanent magnet motors," *IEEE Trans. Energy Convers.*, vol. 32, no. 3, pp. 885-894, Sept. 2017.

[11] A. J. Sorgdrager, R-J. Wang, and A. J. Grobler, "Taguchi method in electrical machine design," *SAIEE African Research Journal*, vol. 108, no. 4, pp. 150-164, Dec. 2017.

[12] R. K. Roy, *Design of experiment using the Taguchi approach*, New York, USA: Wiley, 2001.

[13] R. Jeyapaul, P. Shahabudeen, and K. Krishnaiah, "Quality management research by considering multi-response problems in the Taguchi method - a review," *The International Journal of Advanced Manufacturing Technology*, vol. 26, issue 11-12, pp. 1331-1337, Nov. 2005.

[14] W. Weng, F. Yang, and A. Elsherbeni, "Linear antenna array synthesis using Taguchi's method: A novel optimization technique in electromagnetics," *IEEE Trans. Antennas Propag.*, vol. 55, pp. 723-730, Mar. 2007.

[15] E. Howard and M. J. Kamper, "Weighted factor multiobjective design optimization of a reluctance synchronous machine," *IEEE Trans. Ind. Appl.*, vol. 52, no. 3, pp. 2269-2279, May 2016.

[16] A. J. Sorgdrager, R-J. Wang, and A. J. Grobler, "Retrofit design of a line-start PMSM using the Taguchi method," *IEEE International Electric Machines and Drives Conference (IEMDC)*, Coeur d'Alene, ID, May 2015, pp. 489-495.

[17] A. J. Sorgdrager, R-J. Wang, and A. J. Grobler, "Design optimization of a line-start PMSM considering transient and steady-state performance objectives," *IEEE Energy Conversion Congress and Exposition (ECCE)*, Cincinnati, OH, USA, Oct. 2017, pp. 5057-5064.

[18] R. T. Marler and J. S. Arora, "Survey of multi-objective optimization methods for engineering," *Structural and multidisciplinary optimization*, vol. 26, issue 6, pp. 369-395, Apr. 2004.

[19] R. T. Marler and J. S. Arora, "The weighted sum method for multi-objective optimization: new insights," *Structural and multidisciplinary optimization*, vol. 41, issue 6, pp. 853-862, Jun. 2010.

Albert J. Sorgdrager (S'13-M'17) received the B.Eng and M.Eng degrees in electrical engineering from the North-West University, Potchefstroom, South Africa in 2010 and 2013, respectively, and the Ph.D. degree in electrical engineering from Stellenbosch University, South Africa, in 2017.

Dr. Sorgdrager is currently with Sasol Group Technology: Electrical Engineering Services in Secunda, South Africa. His research interests include line-fed electrical motors, robust and traditional design optimization methods, industrial drive systems.

Rong-Jie Wang (S'00-M'03-SM'08) received the M.Sc. degree in electrical engineering from University of Cape Town in 1998 and the Ph.D. degree in electrical engineering from Stellenbosch University in 2003, all of South Africa.

He is currently an Associate Professor with the Department of Electrical and Electronic Engineering at Stellenbosch university. His research interests include novel topologies of permanent magnet machines, computer-aided design and optimization of electrical machines, cooling design and analysis, and renewable energy systems. Dr. Wang is a co-author of the monograph *Axial Flux Permanent Magnet Brushless Machines* (Springer 2004, 2nd Edition 2008, co-authors: J. F. Gieras and M. J. Kamper).

Andries J. Grobler (M'13) received the B.Eng, M.Eng and PhD degrees in electrical engineering all from the North West University (NWU), Potchefstroom, South Africa, in 2006, 2008 and 2011, respectively. He worked in industry as an electrical engineer in 2011 and joined the NWU in 2012 as a senior lecturer.

His research interests include thermal and electromagnetic modelling of high speed electric machines. Dr. Grobler is a member of the IEEE, SAIEE and a Registered Professional Engineer in South Africa.